Ukrainian Journal of Physical Optics
ISSUE 1
2026

GREEN SYNTHESIS OF SILVER AND SILVER OXIDE NANOPARTICLES FROM *CEDRUS LIBANI*: BIOLOGICAL ACTIVITY AND INFLUENCE OF FILM THICKNESS ON OPTICAL PROPERTIES

ALJOHANI, MESHARI M.[1]*, KHASIM, SYED[2], ALBALAWI, MAHMOUD E.[2], ALFADHLI. S.[2], ALI, MOHAMAD MOUSTAFA[3], WARAKY, AHMED [4,5], DARWICH, NOURHANE A.[6], KHALIL, MAHMOUD I .[6,7] AND HAMDALLA, TAYMOUR A.[2]

[1] Department of Chemistry, Faculty of Science, University of Tabuk, 71491, Tabuk, Saudi Arabia
[2] Department of Physics, Faculty of Science, University of Tabuk, 71491, Tabuk, Saudi Arabia
[3] Department of Medical Biochemistry and Microbiology, Science for Life Laboratory, Uppsala University, SE-751 23 Uppsala, Sweden
[4] Department of Laboratory Medicine, Institute of Biomedicine, University of Gothenburg, Gothenburg, Sweden
[5] Region Västra Götaland, Sahlgrenska University Hospital, Department of Clinical Chemistry, Gothenburg, Sweden
[6] Department of Biological Sciences, Faculty of Science, Beirut Arab University, Beirut, Lebanon
[7] Molecular Biology Unit, Department of Zoology, Faculty of Science, Alexandria University, Alexandria, Egypt
*Corresponding author: mualjohani@ut.edu.sa

Received: 06.10.2025

Abstract. Silver and silver oxide nanoparticles (Ag/AgO-NPs) exhibit remarkable optical and antibacterial properties, making them valuable for a range of industrial and biomedical applications. Synthesis and characterization of Ag/AgO-NPs extracted from *Cedrus libani* leaves with an emphasis on film thickness effects (100, 200, and 300 nm) are reported in this study. The nanoparticles were characterized using photoluminescence (PL), X-ray diffraction (XRD), transmission electron microscopy (TEM), and Fourier transform infrared spectroscopy (FTIR). PL spectra exhibited emission peaks around 400 nm, which are implications of surface defects and phytochemical stabilization. FTIR confirmed the reduction and capping of functional groups, while TEM indicated an average particle size of 20.38 nm (range: 10–40 nm). The peaks at 38.05°, 44.25°, and 64.35° indicate face-centered cubic Ag/AgO NPs, as confirmed by XRD analysis. There was also over 90% transmittance at 1000 nm and above, as well as film thickness-dependent band gaps of 1.22–1.27 eV. Biological assays indicated substantial antibacterial, antioxidant, and antibiofilm activity. Ag/AgO-NPs had minimum inhibitory concentrations of 0.375 mg/mL and minimum bactericidal concentrations of 0.75 mg/mL against *S. aureus* and *E. coli*. The time-kill test showed complete growth inhibition after 24 hours. There was also approximately 41% biofilm inhibition at approximately the sub-doses, and a maximum of 70% of preformed biofilms were killed. Antioxidant activity was assessed. The results showed 59.68% and 77.5% radical scavenging at 100 and 200 µg/mL, respectively. Thus, Ag/AgO-NPs derived from *Cedrus libani* exhibit antimicrobial, antibiofilm, and antioxidant activities, highlighting their promise for both photonic and biomedical applications.

Keywords: silver and silver oxide nanoparticles, film thickness, optical properties, antibacterial activity, photonic and biomedical applications, *Cedrus libani*
UDC: 535.37, 535.34, 58.083
DOI: 10.3116/16091833/Ukr.J.Phys.Opt.2026.01080

1. Introduction

The development of materials science alongside studies in nanotechnology has generated interest in advanced materials with unique properties [1]. The synthesis and application of nanostructured noble metals, particularly silver and silver oxide nanoparticles (Ag/AgO-NPs),

have gained substantial importance regarding their unique biological and optical properties [2, 3]. Due to their distinct optical properties, such as surface plasmon resonance (SPR), strong UV–Vis absorption, and photoluminescence – along with antibacterial functions, Ag/AgO-nanoparticles (NPs) have numerous applications in the biomedical domain, such as in wound dressings, coatings of medical devices, and drug delivery systems [4]. The efficiency and efficacy of Ag/AgO-NPs in antimicrobial and antifungal applications are attributed to their small particle size and high surface area, which, in turn, enhance their reactivity [5]. The functional properties of nanostructures depend on the nanomaterials' surface morphology and crystallinity, which, in turn, are influenced by the nanomaterials' thickness [6, 7, 8].

Green synthesis methods for producing Ag/AgO-NPs have been reported using both physical and chemical processes [9, 10]. Such methods, however, usually require a substantial monetary investment owing to the high energy requirements, high temperatures, high pressures, and expensive machinery. Condensation, sol-gel methods, and reduction, along with other biochemical techniques, are likewise very costly due to the high cost of the expensive metals and solvents, as well as other hazardous reagents and solvents associated with these methods [11]. *Cedrus libani* (*C. libani*), or cedar of Lebanon, is a very tall evergreen tree native to the Eastern Mediterranean. It has been regarded as one of the most important trees in the region because of its medicinal properties since ancient times. It's rich in biochemicals, particularly polyphenolic and terpenoid compounds, which exhibit a considerable level of biological activity. Moreover, these phytochemicals play an essential role in “greener” science by enabling the environment-friendly synthesis of Ag/AgO-NPs [12, 13].

Biological methods for synthesizing Ag/AgO nanoparticles using plant extracts are an important technique in green nanotechnology, particularly because synthesis methods often rely on other, more toxic compounds. It reduces the use of toxic compounds by using plant phytochemicals that can bio-fabricate nanoparticles without altering the biological properties of the source [13]. The field of green nanomaterials for biological applications is rapidly growing, owing to the urgent need for new solutions driven by increasing antibiotic resistance [14]. To this end, the biological properties of Ag/AgO.

NPs have been widely investigated with an emphasis on their antibacterial activity [15]. Understanding the interrelationships among the synthesis parameters, the corresponding structural features, and the resulting properties will aid the development of advanced materials for new applications in technology and medicine. In the present study, we examined the optical and biological properties of Ag/AgO-NPs derived from *C. libani* and investigated the optical characteristics of the nanoparticles, employing the optical methods i.e., we investigated the absorption spectra and refractive index of the prepared nanoparticles thin films with an emphasis on the relationship between film thickness and optical performance parameters, providing critical insight for designing nanomaterials optimized for specific applications.

2. Methodology

2.1. Biosynthesis and thin thickness preparation of Ag/AgO-NPs from C. libani

The biosynthesis of Ag/AgO-NPs was conducted using *C. libani* leaves. Briefly, 0.042 g of the silver nitrate ($AgNO_3$) was added to 250 mL of *C. libani* extract and heated for 30 min at 60°C, as reported previously [16]. The mixture was kept in the dark for 90 min to allow complete reduction of silver ions. A distinct brown color indicated successful biogenic synthesis of silver

nanoparticles. The crude preparation was then centrifuged at 10000 rpm (~9000×g) for 30 min, rinsed, and subjected to a second spin for 15 min before being dried at 40°C in an oven for 24 h. The dried material was weighed to determine the yield of the silver nanoparticles.

The Ag-based nanoparticles were biologically synthesized using the green extract. From this biogenic material, we fabricated thin films via thermal evaporation onto glass substrates to obtain uniform coatings suitable for optical property measurements. The Ag/AgO-NP thin films were fabricated by thermal evaporation under a vacuum of approximately 1.3×10^{-5} Pa, using an HHV Auto 306 coating system and a physical deposition system vapour coating unit for thin film deposition. Thin films of Ag/AgO-NPs with various thicknesses were deposited onto clean glass substrates positioned 15 cm above the evaporator. The evaporation process was conducted at a constant rate of 5 Å/s, with varying evaporation times to achieve the desired film thickness for each sample. Upon completion of the evaporation process, the thickness of the prepared films was measured using the evaporation coating unit. The thicknesses of the resulting films were 100, 200, and 300 nm. The development of Ag and AgO phases can be attributed to the partial oxidation of metallic silver during green synthesis, where the thermal conditions allow bioactive phytochemicals in the extract and atmospheric oxygen to serve as mild oxidizing agents.

2.2. Characterization of the Ag/AgO-NPs

The V-670 UV-Vis spectrophotometer (JASCO, Japan) was used to measure the optical properties of the samples at room temperature over 200-2500 nm. For the NP samples, the supernatant was discarded after the third wash, and the resulting pellet was diluted with distilled water to a concentration that produced a specific color. A 400 µL aliquot of the dilution was transported into a cuvette, which was subsequently filled to the mark with distilled water for the blank measurement.

For the thin films, the optical transmittance and absorbance spectra were recorded directly by placing the coated glass substrates in the UV–Vis spectrophotometer's sample holder, with an uncoated glass slide used as a reference. The same films were also examined by photoluminescence (PL) spectroscopy using a Jasco FP-8600 fluorescence spectrometer equipped with a Xenon laser at 420 nm excitation. Functional groups were identified in the samples using a Nicolet iS5 FTIR-8400S spectrometer, performing Fourier transform infrared spectroscopy (FTIR) at dioxygen at 40°C over 4000–400 cm^{-1}. For FTIR measurement, 2 mg of the sample was mixed with KBr at a 1:100 ratio using a mortar and pestle, then ground and pressed into a disk at 13.79 MPa. Particle morphology was investigated using a high-resolution JEOL JEM-100 CX microscope with a 0.1 nm scale, operating at 80 kV. The images were obtained at a scale of 100 nm. Thereafter, the ImageJ software was used to analyze the particle size distribution from the obtained images.

2.3. Assessment of minimum inhibitory concentration (MIC) and minimum bactericidal concentration (MBC) of Ag/AgO-NPs using the microwell dilution method

The gram-negative and gram-positive bacterial strains of *Escherichia coli* (*E. coli*) and *Staphylococcus aureus* (*S. aureus*), respectively, were cultured in nutrient broth until the turbidity reached the 0.5 McFarland standard. The *E. coli* and *S. aureus* strains used in this study were clinical isolates attained from urine samples and identified using the VITEK® 2 automated identification system. Silver and silver oxide nanoparticles were prepared at final concentrations of 0.0126 mg/mL in a series of two-fold dilutions. Each test well received 90 µL of nutrient broth,

10 μL of the bacterial suspension, and 100 μL of the silver nanoparticle solution. Doxycycline served as the conventional antibiotic positive control. After a 24-hour incubation at 37 °C, optical density (OD) was measured at 595 nm with an ELISA microplate reader, allowing the minimum inhibitory concentration to be defined as the lowest silver concentration that inhibits visible growth. To determine the minimum bactericidal concentration, a loopful of liquid from each clear well was streaked onto Mueller-Hinton agar and incubated at 37 °C for 24 hours; the first concentration without colonies was recorded as the MBC. All assays were achieved in triplicate, as previously reported [17].

2.4. Time-kill assay for biological activity of Ag/AgO nanoparticles

A time-kill assay was used to determine how quickly the silver and silver oxide nanoparticles began to inhibit the bacterial strains under study. In each well, 90 μL of nutrient broth and 10 μL of a bacterial suspension standardized to 0.5 McFarland were mixed. Following this, 100 μL of the nanoparticle concentration that had previously shown a minimum inhibitory concentration was added to the 96-well plate. Then, the plates were incubated at 37°C, and the OD of bacterial growth was monitored and recorded at 595 nm at different time points (0–24 h). The entire procedure was independently repeated three times, and results are reported as mean ± SD to confirm data consistency, as described earlier [16].

2.5. Antibiofilm activity of the Ag/AgO-NPs

Different bacterial strains were cultured in a 96-well microtiter plate by adding 10 μL of a standardized suspension (0.5 McFarland) to each well, comprising 90 μL of nutrient broth. The plates were incubated under static conditions at 37 °C for three hours to allow initial growth. Serial twofold dilutions of green silver and silver oxide nanoparticles, ranging from 0.012 to 6 mg/mL, were then added. Doxycycline was taken as a reference antibiotic, and one well containing only culture medium served as a negative control. The wells were also incubated for 24 h at 37 °C, then washed carefully, dried, and stained with 100 μL of 1% crystal violet for 15 min at room temperature. Purple rings indicating biofilm formation on the sides of the wells appeared after a brief wash. For biofilm quantification, 100 μL of 95% ethanol was added to dissolve the dye, and the reading was taken at 595 nm using an ELISA plate reader.

The following equation was employed to calculate the percentage reduction in biofilm formation:

$$\%\ Inhibition = \frac{OD_{(negative\,control)} - OD_{(treated\,sample)}}{OD_{(negative\,control)}} \times 100\,. \qquad (1)$$

To assess biofilm destruction in the remaining portions of the trials in parallel with other activities, the bacteria were cultivated in nutrient broth, allowing the biofilms to mature for 24 hours before the application of the various experiments. Each independent condition was executed at least three times to ensure that the results were statistically valid [16].

2.6. 2,2-diphenyl-1-picrylhydrazyl (DPPH) assay for antioxidant activity of Ag/AgO-NPs

To evaluate antioxidant activity, different concentrations of Ag/AgO-NPs (between 0 and 200 μg/mL of Ag/AgO-NPs synthesized and mixed with 1 mL of ascorbic acid as a positive control) and 1 mL of 0.3 mM DPPH solution at a ratio of 1:1 were mixed. The negative control was 1 mL of DPPH with 1 mL of methanol. All samples were placed in the dark for 30 min and then analyzed by a spectrophotometer at 517 nm. All experimental treatments were performed in triplicate to assess reproducibility and minimize the contribution of systematic

and random errors to the data set [17].

The DPPH radical scavenging efficiency was quantified according to the relationship expressed in the equation below:

$$DPPH\ radical\ scavenging\ activity\ (\%) = \frac{A_c - A_s}{A_c} \times 100, \quad (2)$$

where A_c is the absorbance of the control, and A_s is the absorbance of the sample.

Statistical analyses were performed using Microsoft Excel, graphs were organized with Origin software, and significance was evaluated through Student's *t*-tests. All biological experiments were carried out in triplicate (n = 3).

3.3. Results and Discussion

3.1. Photoluminescence studies

The optical properties and electronic configuration of the Ag/AgO-NPs were evaluated by studying the NPs' PL spectrum. According to Fig. 1, the Ag/AgO-NPs exhibited a significant emission peak in the UV-visible region, which may be attributed to surface defects [18]. The recorded PL spectrum of the biosynthesized Ag/AgO nanoparticles shows a broad emission band with a peak at ~436 nm. This emission peak may result from radiative recombination at the Ag/AgO interface and at Ag/AgO defect trap states. The surface photoluminescence can primarily be due to the oxide-phase defects (oxygen vacancies), with organic phytochemicals from the extract possibly stabilizing these defect centers and thus suppressing the non-radiative recombination of the surface photoluminescence [16]. The observed PL emission suggests their potential for bioimaging applications, pending further evaluation of stability and biocompatibility [19].

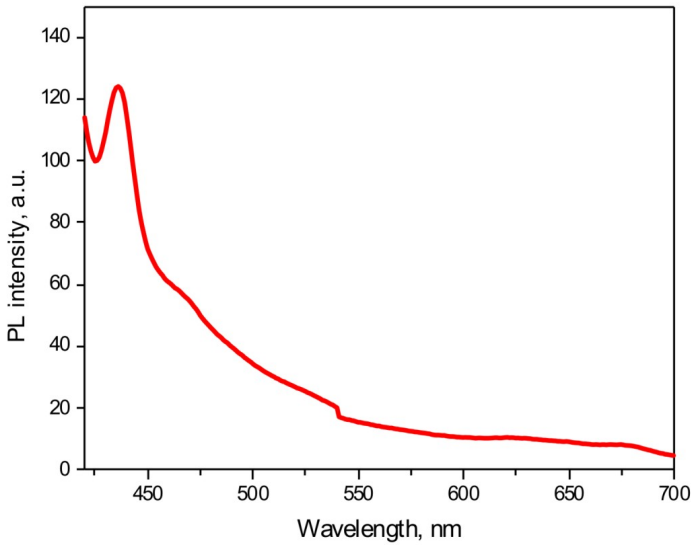

Fig. 1. Photoluminescence spectra for Ag/AgO-NPs.

3.2. FTIR analysis

The FTIR spectrum of the biosynthesized Ag/AgO-NPs revealed distinct peaks due to the various functional groups that play a vital role in stabilization and reduction processes. Fig. 2 shows the FTIR spectra of green-synthesized Ag/AgO-NPs. A broad peak at 3423 cm^{-1} was assigned to the O–H stretching vibrations associated with phenolic and alcoholic groups, signifying the presence of polyphenols in the plant extract, which most likely acted as

reducing agents. The peaks appearing at 2919 and 2360 cm^{-1} were assigned as C–H stretching and atmospheric CO_2, respectively [16]. The peak at 1637 cm^{-1} was assigned to C=O, arising from amide I in the protein or carbonyl groups in the polyphenols in the extract, which are responsible for capping nanoparticles. Also, the bands at 1509 and 1046 cm^{-1}, assigned to aromatic C=C and C–O–C vibrations, respectively, further supported the notion that the stabilizing secondary metabolites bound to the nanoparticles [20]. The Ag–O bond vibrations attributable to the AgO nanoparticles formed were peaking at 659 cm^{-1}. These results indicate that the phytochemicals in the extract served as reducing and capping agents, consistent with other literature on green synthesis routes.

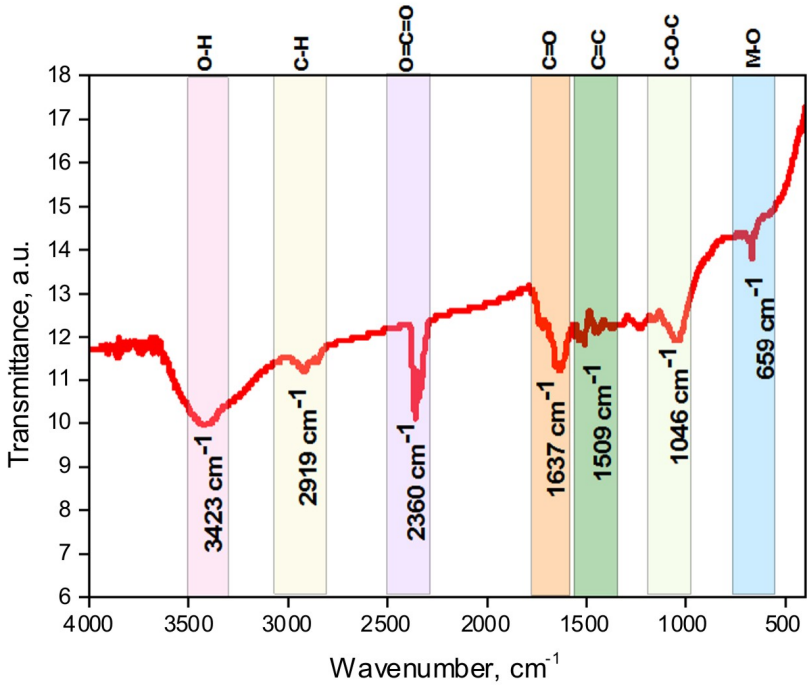

Fig. 2. FTIR spectra for green-synthesized Ag/AgO-NPs.

3.3. Transmission electron microscopy (TEM) analysis

Nanoparticle morphology was assessed using TEM. Fig. 3 illustrates that the biosynthesized Ag/AgO-NPs are predominantly spherical, exhibit a narrow size distribution, and show considerable separation, indicating successful surface capping by the phytoconstituents in the plant extract. The analysis of the size distribution histogram revealed that most Ag/AgO-NPs were within the 10-40 nm range, with an average particle size of approximately 20.38 nm. Minimal aggregation also supported the stabilizing effect of biomolecules during synthesis. The obtained results align with other research reporting spherical Ag/AgO-NPs synthesized using pine needle leaf extract, with diameters less than 50 nm [16]. Extremely small and narrowly distributed sizes, in turn, imply a greater surface proportion of the Ag/AgO-NPs, which enhances biological activity and membrane interactions with microbes. These properties verified the green synthesis of Ag/AgO-NPs, providing the particles with appropriate nanoscale characteristics for biomedical applications. TEM analysis confirmed the nanoscale morphology and uniform distribution of the Ag/AgO-NPs. Although TEM does not itself prove green synthesis, the use of C. libani leaf extract as the reducing and

stabilizing agent, along with FTIR evidence of phytochemical functional groups on the nanoparticle surface, supports the successful green synthesis of Ag/AgO-NPs with suitable characteristics for biomedical applications.

The TEM images confirmed both the spherical shape and the size distribution of the particles synthesized at the nanoscale. However, the morphological characteristics are not, by themselves, proof of synthesis by green methods. That the synthesis was biogenic was confirmed by FTIR spectra, which showed distinct peaks, indicating the presence of strongly hydroxyl, carbonyl, and phenolic groups from the pine needle extract, substantiating their involvement in the reducing and capping processes occurring in the nanoparticles. The synthesized Ag/AgO nanoparticles exhibit some interesting properties necessary for their desired uses in biomedicine; however, their cytotoxicity, biocompatibility, and stability under physiological conditions still need to be further investigated.

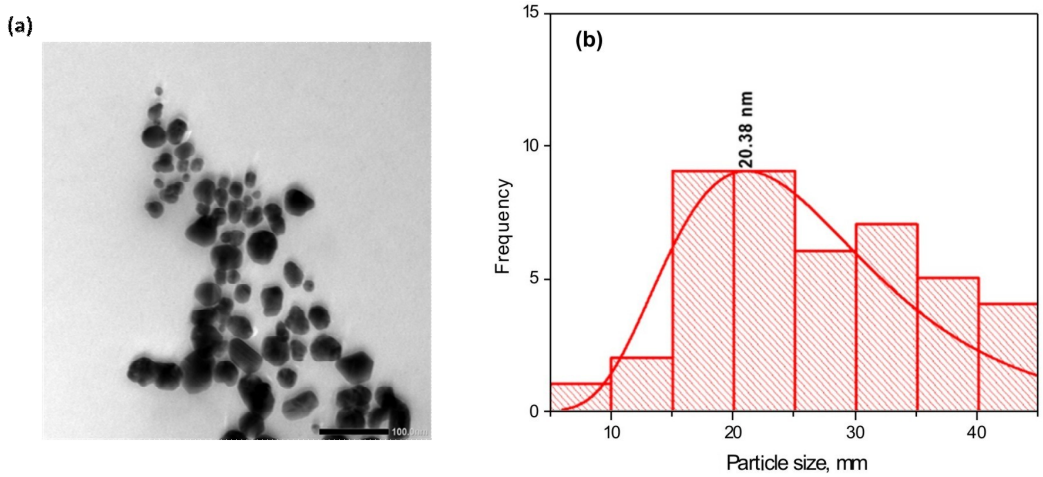

Fig. 3. (a) TEM images and (b) histogram of the particle size distribution of the biosynthesized Ag/AgO-NPs.

3.4. X-ray diffraction (XRD) analysis

The XRD was used to examine the crystallographic structure of the Ag/AgO-NPs. As shown in Fig. 4, the XRD of the biosynthesized Ag/AgO-NPs demonstrated peaks at (27.2°, 32.1°, 38.05°, 44.25°,46.2°, 64.35°, and 77.35°). The most intense peaks appearing near 38.05°, 44.25°, and 64.35° can be attributed to the (111), (200), and (220) planes of face-centered cubic (*fcc*) metallic silver (Ag), and the weaker reflections near 32.1° and 46.2° correspond to the tetragonal AgO phase. The weak diffraction patterns at 27.2° and 77.35° may be interpreted as lattice strain or as mixed Ag/AgO interfacial phases, as commonly observed in partially oxidized Ag systems. These results also attest that the biosynthesized nanoparticles have a composition of both phases (metallic silver and silver oxide). The data therefore indicate a mixture of metallic Ag and silver oxide(s), which is common for biosynthesized and thermally-processed samples where partial reduction can occur. XRD peaks confirm that the nanoparticles possess a well-developed crystalline structure. The presence of sharp XRD peaks indicates a high degree of crystallinity, enhancing the structural stability and uniformity of the nanoparticles. These features affect the surface reactivity and the biological behavior of the nanoparticles, which may contribute to the observed antimicrobial activity. Such structural order can also support desirable optical properties, making these nanoparticles valuable for applications [21]. The sizes of the biosynthesized Ag/AgO-NPs

were confirmed based on the XRD data, and were calculated based on the Scherrer Eq. (3) as indicated below:

$$D = \frac{K\lambda}{\beta \cos\theta}, \tag{3}$$

where D is the average crystallite size, K is Scherrer's constant (K = 0.9), λ is the X-ray wavelength, β is the line broadening at FWHM, and θ is the Bragg angle. Using the Scherrer equation, the average crystallite size obtained is approximately 20.38 nm, confirming the presence of well-developed crystalline domains within the Ag/AgO-NPs extract. The relatively narrow diffraction peaks suggest good crystallinity and efficient extraction and purification processes employed during Ag/AgO-NPs production from plant sources.

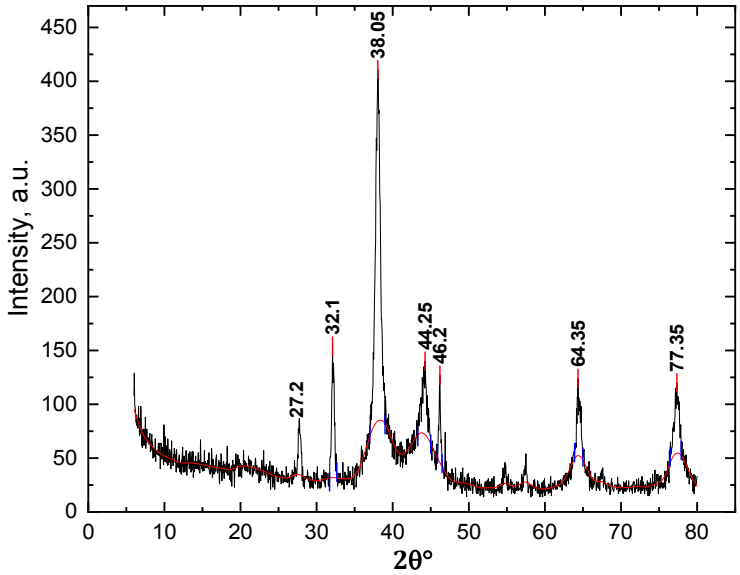

Fig. 4. XRD of the biosynthesized Ag/AgO-NPs.

3.5. Optical properties investigation

The optical transmission and reflection spectra of the Ag/AgO-NP thin films were recorded using a UV–VIS spectrophotometer. The spectral distributions of optical transmittance (T) and reflectance (R) for Ag/AgO NPs extracted from *C. libani* are presented in Fig. 5, demonstrating several significant optical characteristics that merit detailed analysis. This figure shows two regions: the first corresponds to longer wavelengths (λ > 1000 nm), where thin films are transparent, and no light is scattered or absorbed (R+T=1).

The refractive index (n) spectral characteristics, excavated from *C. libani* Ag/AgO-NPs thin films, are calculated using:

$$n = \left(\frac{1+R}{1-R}\right) + \sqrt{\frac{4R}{(1-R)^2} - k^2}, \tag{4}$$

where k is the Extinction coefficient, which can be calculated as k=$\lambda\alpha/4\pi$, the calculated n is shown in Fig. 6, demonstrating the typical characteristics of semiconductor and oxide thin films. Normal dispersion behavior is shown in the visible region of the spectrum, while anomalous dispersion is present in the region near the absorption edge. The refractive index measures the relative electronic polarizability of various bonds, relative to their covalent

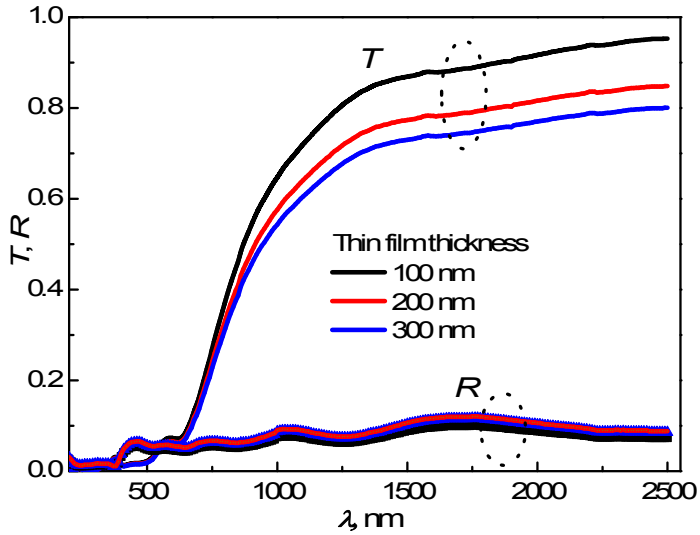

Fig. 5. The spectral distribution of transmittance, *T*, and reflectance, *R*, for Ag/AgO -NPs films with different thicknesses.

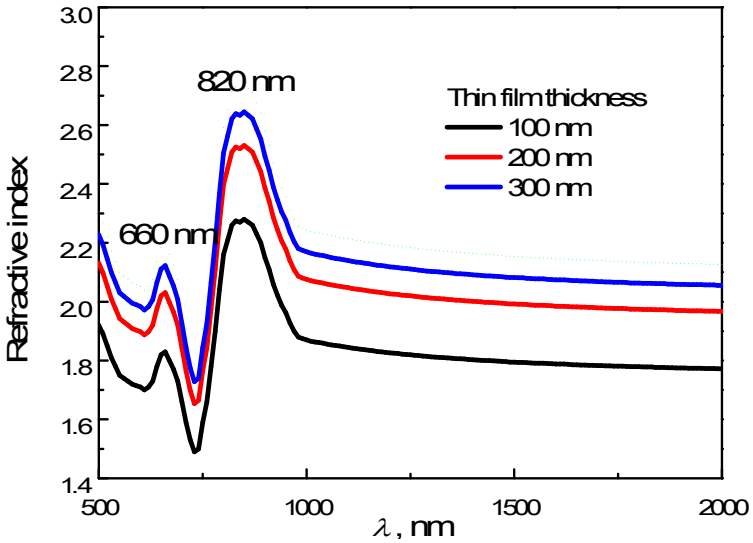

Fig. 6. Spectral behavior of refractive index (*n*) of Ag/AgO -NPs thin films with different thicknesses.

bond strengths, to determine the material's optical response. This is well aligned with the transmittance and reflectance spectra in Fig. 5, which show a physical interdependence. In this context, the phytochemical components present in *C. libani*, including phenolic, terpenoid, and flavonoid compounds, may serve as capping and reducing agents during nanomaterial formation, resulting in the observed optical properties [22].

As depicted in Fig. 7, the variation of $(n^2\text{-}1)^{-1}$ with $(h\nu)^2$ for Ag/AgO-NPs films with different thicknesses can be described in terms of the dielectric response for transitions below the optical gap. Values E_o (single-oscillator energy, which represents the average energy gap of electronic transitions) and E_d (dispersion energy, which represents the strength of interband optical transitions) were calculated from the slope and intercept of a plot of $1/(n^2-1)$ versus $(h\nu)^2$ in Fig. 7. Also, the refractive index can be utilized to determine the lattice dielectric constant (ε_L), which accounts for the lattice model as well as free

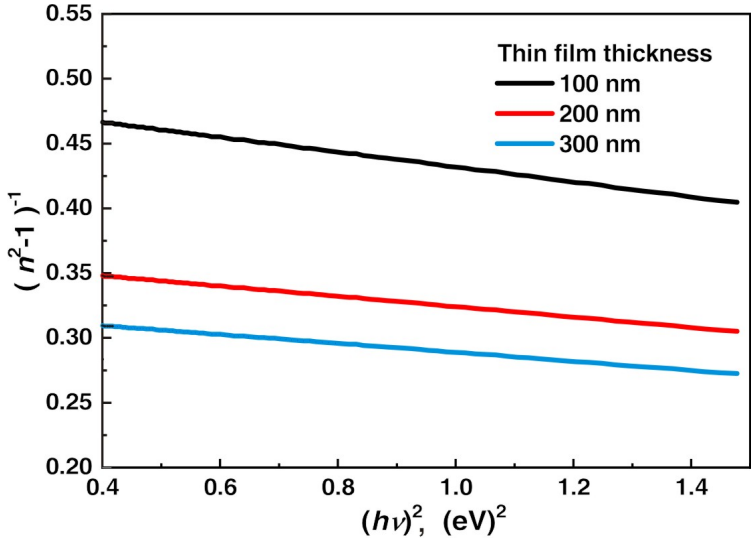

Fig. 7. Variation of $(n^2\text{-}1)^{-1}$ with $(h\nu)^2$ for Ag/AgO-NPs films with different thicknesses.

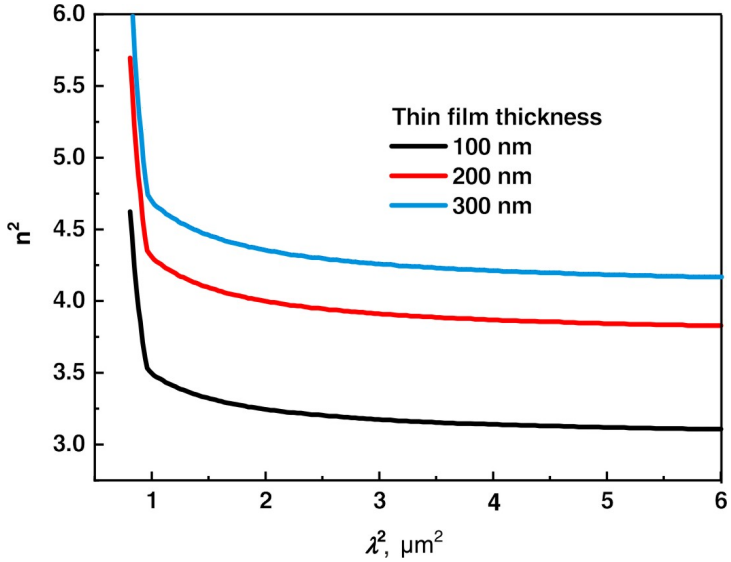

Fig. 8. The relation between n^2 and λ^2 for *C. libani* – Ag/AgO-NPs films with different thicknesses.

carriers for dispersion. The connectivity between wavelength (λ) and the real part of the dielectric constant (ε_1) in the normal dispersion region is given by [23]:

$$\varepsilon_1 = n^2 = \varepsilon_L - \frac{e^2}{4\pi^2\varepsilon_o c^2}\frac{N}{m^*}\lambda^2, \quad (5)$$

where e is the elementary charge, ε_o is the permittivity of free space, and N/m^* is the ratio of free carrier concentration to free carrier effective mass. The relationship between n^2 and λ^2, as displayed in Fig. 8, further elucidates the dispersion behavior of these nanomaterials using the Wemple–DiDomenico (W–D) model. The linear plots for different thicknesses show normal dispersion, with the refractive index decreasing with increasing wavelength. The relationship observed with thickness indicates that changes in film density, defect concentration, and phase composition affect the electronic polarizability of Ag/AgO nanoparticles.

The optical absorption coefficient (α) of the Ag/AgO nanocomposite was calculated using the relation:

$$\alpha = \frac{4\pi k}{\lambda}, \tag{6}$$

where k – is the extinction coefficient. Fig. 9 shows that the absorption coefficient is approximately 10^4 cm^{-1}. It is also evident that the absorption coefficient increases with increasing film thickness. The sharp increase in absorption at specific photon energies corresponds to electronic transitions from the valence band to the conduction band, providing insights into the band gap energy.

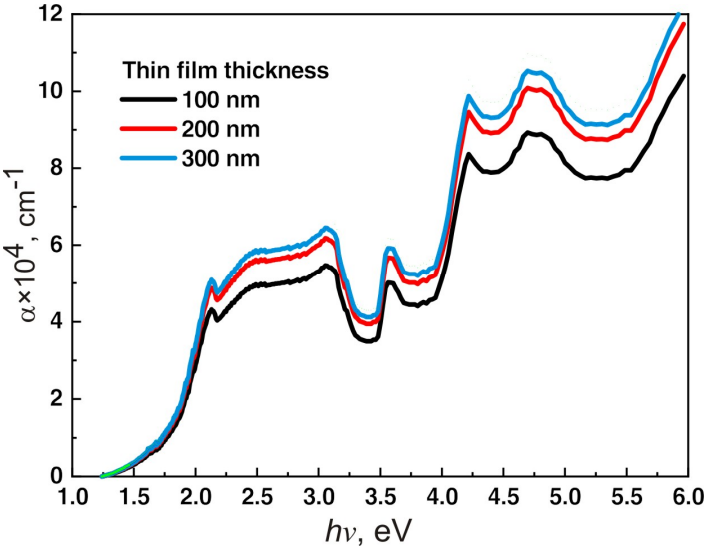

Fig. 9. Spectral behavior of absorption coefficient (α) as a function of photon energy ($h\nu$) for *Cedrus libani* – Ag/AgO-NPs films with different thicknesses.

The kind of electron transition and optical energy gap values were determined by utilizing the Tauc (Davis–Mott) formulation [24]:

$$(\alpha h\nu)^r = B\left(h\nu - E_g\right), \tag{7}$$

where B, E_g, and r are specific constants associated with level splitting and electronic conductivity, the energy gap, and a value, which signifies a process of transition, respectively. In this, r refers to a constant that depends on the nature of band-to-band electronic transitions and the profiles of the valence and conduction band electron densities.

The results of the experiment with varying values of r were fitted to Eq. 5, r=1/2 (indirect allowed transitions), which gave the better fit. This performance was modified using the following equation:

$$(\alpha h\nu)^{1/2} = B(h\nu - E_g \pm E_{ph}), \tag{8}$$

where E_{ph} is the phonons-assisted energy. Fig. 10 shows the variation of $(\alpha h\nu)^{1/2}$ with $(h\nu)$ for *C. libani* – Ag/AgO-NPs films with different thicknesses. The Tauc plots show two regions, which may indicate the presence of direct and indirect optical transitions. The indirect transition is associated with the lower-energy band gap (E_{g1}), while the higher-energy band gap (E_{g2}) is due to the direct transition of the mixed Ag/AgO nanostructures. The values of the optical energy gap are 1.22, 1.25, and 1.27 eV for 100 nm, 200 nm, and 300 nm, respectively. This means that the optical energy gap depends on film thickness. The range of optical gaps can vary due to any of the reasons above, with an increase in structural bonding

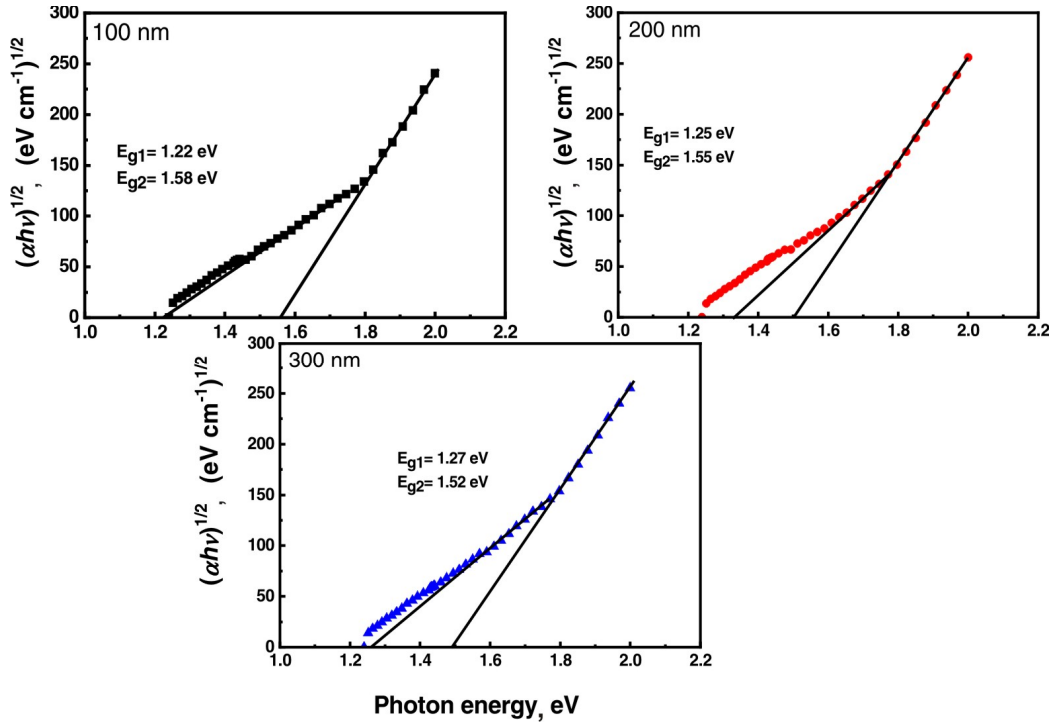

Fig. 10. Variation of $(\alpha h\nu)^{1/2}$ with $(h\nu)$ for *C. libani* Ag/AgO-NPs films with different thicknesses.

disorder and crystal field distortions due to structural defects from increased film thickness being the most critical [25]. The tail of the absorption edge shows the appearance of localized states, which is normal for indirect transitions in nanocrystalline materials or amorphous structured materials. The observed thickness dependence of the band gap energy reveals that the measured Eg values increase with thickness (1.22 → 1.27 eV for 100 → 300 nm). This behavior is characteristic of nanoscale materials and differs significantly from bulk Ag and AgO-NPs. The extent of tailing is determined, to a first approximation, through plotting the edge data absorption; this technique has been applied to different crystalline materials.

Fig. 11 depicts the linear dependence of the natural logarithm of the absorption coefficient relative to the photon energy. Urbach tails exhibit exponential behavior at lower photon energies, suggesting the presence of localized states that penetrate the band gap. The linear portions from which slopes may be taken calculate the Urbach energy. The observation that the Urbach energy decreases with increasing film thickness suggests that structural disorder and defect states become less prevalent. In a fuller explanation, thicker films yield superior crystal quality, with fewer defects and band-tail states, as their surface-to-volume ratio decreases [26].

The inverse of the slope gives the tail width. Thus, the localization of states increases with increasing differential film thickness. To describe light absorption by non-solid molecular media, we need a relationship between the absorption coefficient (α) and the molar extinction coefficient (ε_{molar}). The values ε_{molar} were calculated as [25]:

$$\varepsilon_{molar}\left(L\text{mol}^{-1}\text{cm}^{-1}\right)=\frac{M\alpha}{\rho\times10^{3}\ln(10)}, \tag{9}$$

where ρ and M represent the density of the solid mass and its molecular weight, respectively.

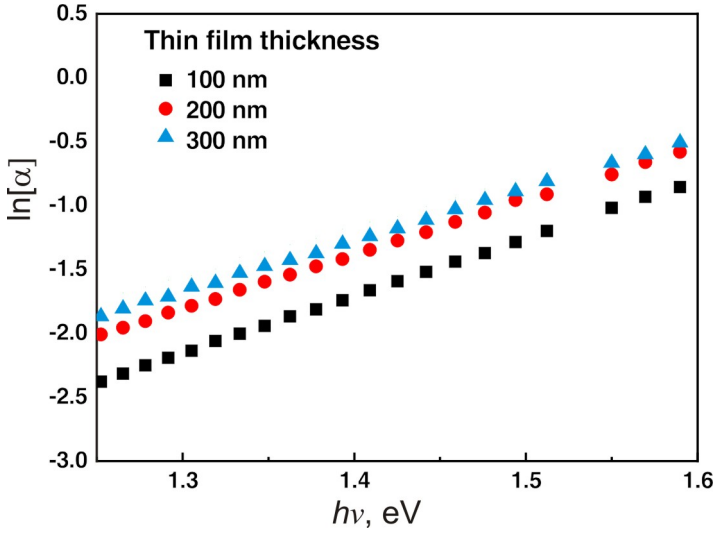

Fig. 11. Dependence of ln(α) on *hν* for *C. libani* – Ag/AgO-NPs films with different thicknesses.

The molar extinction coefficient (ε_{molar}) as a function of photon energy ($h\nu$) for C. libani Ag/AgO-NPs thin films with different thicknesses is shown in Fig. 12. It shows three main absorption regions, which we will designate as 1, 2, and 3. Absorption Region 1 (4.8–5.2 eV) corresponds to interband electronic transitions between the valence band and the conduction band of metallic silver (Ag). It can therefore be assigned to transitions involving metallic silver (Ag). Absorption Region 2 (4.0–4.4 eV) describes charge-transfer transitions about Ag–O bonds in

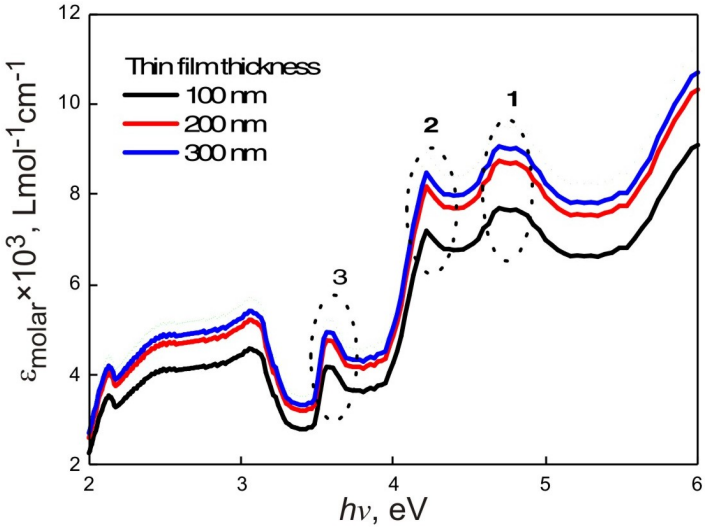

Fig. 12. The molar extinction coefficient (ε_{molar}) as a function of photon energy ($h\nu$) for *C. libani* Ag/AgO-NPs films with different thicknesses.

the AgO phase. Absorption Region 3 (3.3–3.8 eV) likely corresponds to the localized SPR excitations as well as defect-activated transitions due to oxygen deficiencies in the mixed Ag/AgO structure. The film's increased thickness is correlated with the increased intensity of these features, which is indicative of improved film densification and enhanced light–matter interaction.The ε_{molar} has been used to calculate the important parameters such as the oscillator strength (f) and the electric dipole strength (q^2) according to [27]:

$$f = 4.32 \times 10^{-2} \int \varepsilon_{molar}(\upsilon) d\upsilon \,, \tag{10}$$

$$q^2 = \frac{\Delta\lambda}{2500\,\lambda} \varepsilon_{molar} \,, \tag{11}$$

where $\Delta\lambda$ denotes the absorption half bandwidth.

The rise in calculated oscillator strength (f) values with increasing film thickness suggests more robust electronic transitions and enhanced dipole interplay within the Ag/AgO nanostructure. In the same manner, the electric dipole strength (q^2) displayed analogous behavior, correlating with the impact of localized SPR phenomena at the nanoscopic level. The observed peaks in the molar extinction coefficient correspond to specific electronic transitions, with higher values indicating stronger absorption. The thickness dependence of these peaks suggests that the electronic transitions are influenced by surface plasmon resonances characteristic of noble-metal nanostructures. Visible spectra (approximately 400-700 nm) achieved high molar extinction coefficients, demonstrating strong photon absorption.

3.6. Minimum inhibitory concentration for C. libani Ag/AgO-NPs

The microdilution technique was used to determine the MIC of silver and silver oxide nanoparticles against *E. coli* and *S. aureus* and to evaluate the antibacterial activity of *C. libani* Ag/AgO-NPs. Fig. 13 shows that, for both bacterial strains, there was a significant dose-dependent decrease in OD, indicating growth inhibition that increased with higher nanoparticle concentrations.

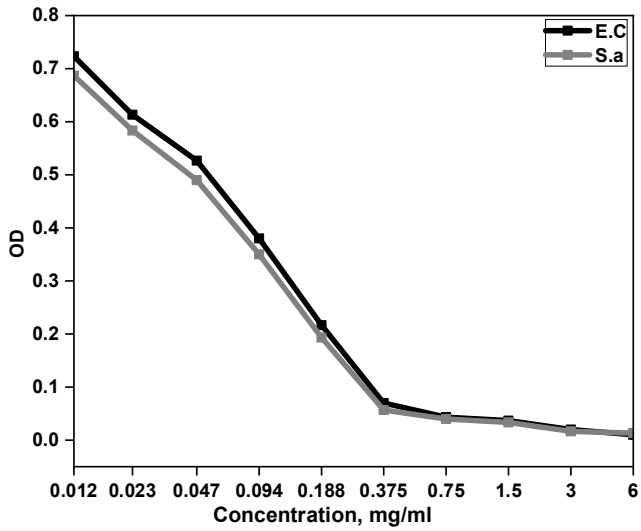

Fig. 13. MIC of *C. libani* Ag/AgO-NPs determined by OD for *E. coli* and *S. aureus*.

E. coli and *S. aureus* exhibited OD readings of approximately 0.74 and 0.68, respectively, at the lowest tested concentration (0.012 mg/ml). As the concentration increased, OD values decreased correspondingly, with a sustained reduction in bacterial growth starting at about 0.094 mg/ml and near-baseline OD values (~0.08) observed at higher concentrations (≥1.5 mg/mL). For the two strains tested, the minimum inhibitory concentration, defined as the lowest dose that inhibits bacterial growth, ranged from 0.188 to 0.375 mg/mL, with 0.375 mg/mL reducing bacterial growth by roughly 60% of the initial OD at 0.188 mg/mL. While *S. aureus* and *E. coli* showed almost identical overall responses to Ag/AgO-NPs,

S. aureus proved more sensitive at lower doses, as evidenced by consistently lower OD readings. This finding aligns with earlier reports indicating that many gram-positive species respond more quickly than gram-negative species to certain nanoparticle treatments, a difference likely due to the distinct structures of their cell walls [17]. Ag/AgO-NPs displayed strong antimicrobial activity against both gram-negative and gram-positive bacteria. Their mechanism likely involves damaging cell membranes, inducing oxidative stress, and disrupting cellular functions and biomolecules [28].

3.7. Minimum bactericidal concentration for C. libani Ag/AgO-NPs

MBC determined for the green-synthesized Ag/AgO-NPs were 0.75 mg/mL against both *E. coli* and *S. aureus*. At this concentration, no colonies appeared on the agar plates, indicating complete killing; however, lower concentrations still permitted visible growth (Fig. 14). Of note, the ratio of the minimum bactericidal concentration (0.75 mg/mL) to the minimum inhibitory concentration (0.375 mg/mL) indicates that the nanoparticles exhibit substantial bactericidal activity, even when administered at comparatively modest doses (Table 1). The Ag/AgO-NPs can kill both gram-negative and gram-positive strains and therefore serve as alternative antimicrobial agents worthy of further exploration. Qanash H. et al. [29] also reported comparable results, demonstrating that biogenic silver nanoparticles have an MBC/MIC ratio of 2 or less, confirming significant bactericidal activity. Furthermore, the effectiveness of green-synthesized nanoparticles is well established and widely documented, primarily due to their disruptive effects on microbial membranes and their ability to generate reactive oxygen species [30].

Fig. 14. MBC for *C. libani* Ag/AgO-NPs for *E. coli* and *S. aureus*.

Table 1. MICs and MBCs for *C. libani* Ag/AgO-NPs.

Bacteria	MIC	MBC	MBC/MIC	Susceptibility
Gram-negative *E. coli*	0.375	0.75	2	Bactericidal
Gram-positive *S. aureus*	0.375	0.75	2	Bactericidal

Note: Ag/AgO-NPs = silver and silver oxide nanoparticles. Abbreviations: MIC = minimum inhibitory concentration, MBC = minimum bactericidal concentration, S= Susceptible.

3.8. Time kill test for C. libani Ag/AgO-NPs

In the time–kill experiment, viable counts for *E. coli* and *S. aureus* followed a biphasic trend: the first three hours were characterized by an initial transient growth with a resultant

decrease throughout the course of the assay (Fig. 15). OD at 0 hours was identical for both cultures, having a reading of 0.10, thereby ensuring identical inoculum density. After 60 min of exposure, OD values advanced imperceptibly to 0.15 and 0.13 for *E. coli* and *S. aureus*, respectively. At a 2-hour interval, maximal ODs of 0.33 for *E. coli* and 0.29 for *S. aureus* were determined. The observed initial increase, therefore, suggests a period of permissive growth during which only marginal inhibitory activity was observed against both strains. At 3 hours, OD increased to 0.36 for *E. coli* and to 0.31 for *S. aureus*, evidencing the onset of bacterial growth. The maximal inhibitory effect was measured at 24 hours of constant exposure, at which time OD values had dropped to 0.08 and 0.03 for *E. coli* and *S. aureus*, respectively. This progressive decline throughout the incubation period reflects cumulative bactericidal activity, reaching a plateau at which the majority of cellular metabolic activity and/or structural integrity were compromised. The findings confirm that *C. libani*–derived Ag/AgO-NPs are effective bactericidal agents, as evidenced by a decrease in OD, indicating bacterial growth inhibition. The NPs efficacy against both gram-negative *E. coli* and gram-positive *S. aureus* indicates broad-spectrum activity. Such rapid antimicrobial activity within 24 h has been reported [16], and Girma et al. demonstrated that nanoparticle-induced oxidative stress causes irreparable membrane damage in these bacteria, supporting the observed activity of Ag/AgO-NPs [31].

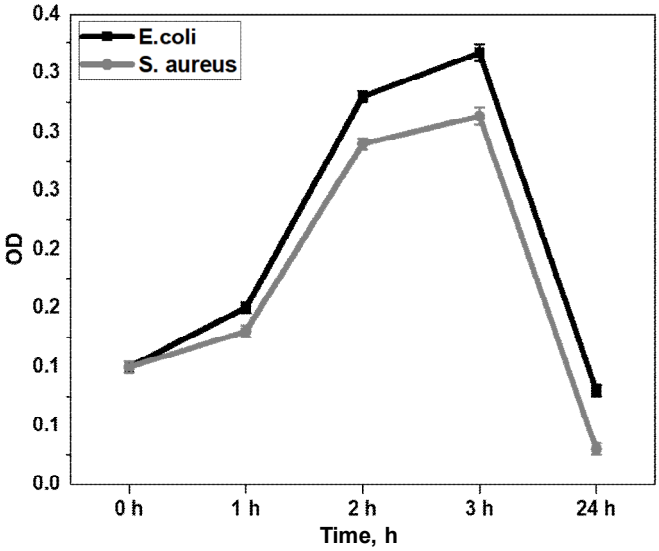

Fig. 15. Time kill test for *C. libani* Ag/AgO-NPs against *E. coli* and *S. aureus*.

3.9. Biofilm formation for C. libani Ag/AgO-NPs

Concentrations ranging from 0.012 to 6 mg/mL of silver and silver oxide nanoparticles (Ag/AgO-NPs) were evaluated for biofilm formation for both gram-negative and gram-positive bacteria, *E. coli* and *S. aureus*, respectively. Biofilm formation results indicated a measurable decrease in biofilm biomass with increasing concentrations of nanoparticles (Fig. 16). At the lowest concentrations (0.012–0.047 mg/mL), the inhibition was moderate, ranging from 16.17 -17.87 % for *S. aureus* and 7.74-32.06 % for *E. coli*. As the concentration increased to 0.094–0.188 mg/mL, inhibition became more evident, with *E. coli* showing 24.17-29.77 % inhibition and 21.50-27.26 % for *S. aureus*. Inhibition then increased progressively at the MIC (0.375 mg/mL), reaching 37.66 % for *E. coli* and 32.92 % for

S. aureus.It is well-documented that silver nanoparticles can inhibit biofilm formation in *S. aureus* and *E. coli*. Darwich et al. and Khaldoun et al., for example, demonstrated that silver nanoparticles disrupted biofilm formation through the disruption of quorum-sensing pathways, which are integral to biofilm formation [16], [32]. Similarly, E. O. Mikhailova and colleagues demonstrated that silver nanoparticles compromised bacterial adhesion and stressed the bacteria, leading to loss of the EPS matrix [33]. The mechanisms that were proven to enhance biofilm inhibition agree with Ag/AgO-NPs disrupting bacterial biofilm formation by attacking intercellular communication and structural damage [33].

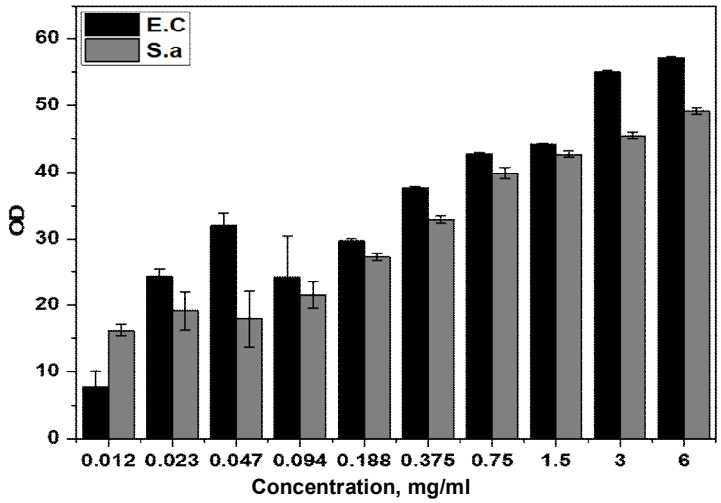

Fig. 16. Biofilm inhibition activity of *C. libani* Ag/AgO-NPs against *E. coli* and *S. aureus*.

3.10. Biofilm eradication for C. libani Ag/AgO-NPs

The ability of the nanoparticle to disrupt pre-formed biofilms was assessed in vitro using *E. coli* and *S. aureus* over a wide concentration range, with results presented in Fig. 17. No statistically significant biomass reduction was observed at the lowest concentration tested (0.012 mg/ml). Experimental measurement revealed a moderate, transient increase in

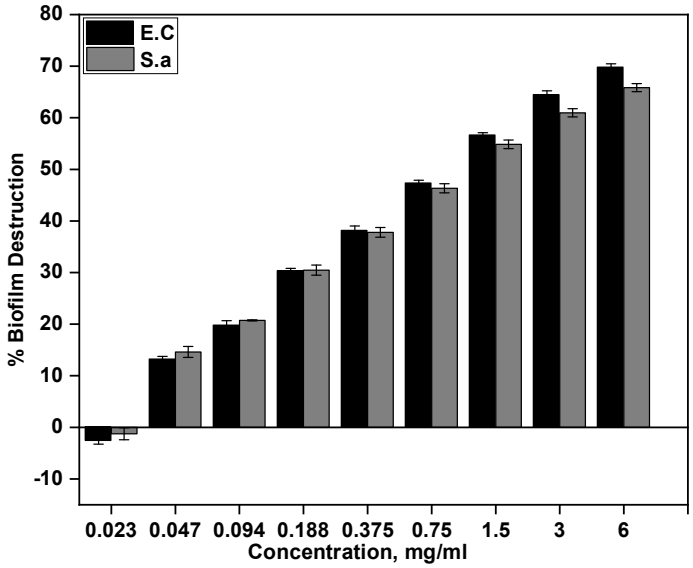

Fig. 17. Biofilm eradication activity of *C. libani* Ag/AgO-NPs against *E. coli* and *S. aureus.*

biofilm, an effect most likely due to minor, sub-lethal stress that transiently up-regulated protective extracellular polymeric substances [34]. A clear threshold was achieved at 0.047 mg/ml, where both test species indicated a reduction of approximately 15–20 %, the first observable activity against the matrix. From 0.094 to 0.375 mg/ml, the material removal rate increased stepwise, reaching only a little over 40 % at the upper end of the range, suggesting greater molecular penetration or adhesin disruption of the surface rather than cell killing *per se*. Concentrations above 0.75 mg/ml consistently killed over 45 % of mature biofilm, and 6 mg/ml achieved optimal values for 70 % of *E. coli* and 65 % of *S. aureus*, demonstrating a dose-dependent interaction. Surprisingly, *E. coli* proved marginally more sensitive than *S. aureus*, especially at concentrations of 1.5 mg/ml and above; however, the broader response patterns for both organisms remained parallel throughout the study. The present findings are consistent with earlier reports suggesting that nanoparticle-based agents can eradicate mature biofilms by degrading the extracellular matrix, inducing oxidative stress, and disrupting bacterial signaling mechanisms [35].

Current research supports earlier work demonstrating that biofilm-eradicating nanoparticle-based agents can kill mature biofilms by degrading the biofilm matrix, inducing oxidative stress, and disrupting bacterial communication pathways [34]. Hosnedlova et al. also demonstrated the same with silver nanoparticles, reducing biofilm mass in *E. coli* and *S. aureus* by a considerable amount through disruption of the cell wall and EPS structures [36]. In addition, Mohanta et al. demonstrated that green-synthesized silver nanoparticles suppressed mature *S. aureus* and *E. coli* biofilms by inducing ROS production and disrupting quorum sensing [37].

3.11. Antioxidant activity for C. libani Ag/AgO-NPs

The DPPH assay results confirmed the antioxidant activity of the synthesized Ag/AgO-NP thin film, indicating a concentration-dependent increase in scavenging activity. As shown in Table 2. At 100 μg/mL, the scavenging activity was 59.68 %, and it increased to 77.5 % at

Table 2. Antioxidant potential of *C. libani* Ag/AgO-NPs against DPPH.

Concentration, μg/mL	**Percentage of DPPH activity, %**	
	Ag/AgO-NPs	**Ascorbic acid**
0	0.0 ± 0.00	0.0 ± 0.00
p-value	-	-
Significance	-	-
25	19.51 ± 0.44	22.17 ± 0.28
p-value	0.000765	0.000248
Significance	***	***
50	37.25 ± 0.72	42.49 ± 0.48
p-value	0.00063	0.000194
Significance	***	***
100	59.68 ± 1.20	69.12 ± 0.24
p-value	0.001452	1.05E-05
Significance	**	***
200	77.50 ± 0.58	91.13 ± 0.10
p-value	0.00381	2.14E-06
Significance	**	***

Note that: DPPH = 1,1-diphenyl-2-picrylhydrazyl; S = significance; — = not determined.
*p < 0.05, ** p < 0.01, *** p < 0.001.

200 μg/mL. This indicates that, up to 200 μg/mL, the nanoparticles still exhibit increasing scavenging activity, and thereafter a plateau is reached. The concentration-dependent bioactivity of the ascorbic acid positive control did indeed verify the assay, as it showed 69.12 % scavenging at 100 μg/mL and 91.13 % at 200 μg/mL. This suggests that the maximum radical-scavenging capacity is likely reached at or slightly above 200 μg/mL, probably because all available DPPH radicals had been saturated. The observed trend reinforces the hypothesis that biosynthesized nanoparticles are effective antioxidants due to bioactive phytochemicals, which are hypothesized to cap their surfaces [38]. These results corroborate those of other researchers focusing on green nanoparticles and emphasize once again the importance of plant-derived functional groups for free radical scavenging [39].

4. Conclusion

The study continues to demonstrate the effective green synthesis of silver and silver oxide nanoparticles (Ag/AgO-NPs) from the leaves of *C. libani* and to report the optical, structural, and biological characteristics of the resultant nanomaterials. The Ag/AgO-NPs had an average diameter of ∼20 nm, exhibited intense PL at 436 nm, high crystallinity, and high optical transmittance (>90%) along with thickness. Stabilization by phytochemicals was confirmed by FTIR, and crystalline integrity was confirmed by XRD. Remarkably, Ag/AgO-NPs exhibited strong antibacterial and antibiofilm properties. MICs and MBCs of Ag/AgO-NPs were 0.375 and 0.75 mg/mL, respectively, against *S. aureus* and *E. coli*, and at high concentrations, biofilm killing was >70 %. After 24 hours, time-kill assays indicated total suppression. Antioxidant assays also showed dose-dependent radical scavenging activity. These results place Ag/AgO-NPs among the most promising nanomaterials for both biomedical and technological applications. Their use in renewable devices, bioimaging equipment, and antimicrobial films is promising to a certain extent and thus is a good candidate for future applications where sustainability, tunability, and therapeutic activity are equally desirable.

Author Contributions. Aljohani, Meshari M.: Writing, Reviewing, and supervising; **Khasim, Syed:** Investigation, Analysis, and writing; **Albalawi, Mahmoud E.:** Writing and Reviewing; **Alfadhli, S.:** Investigation and reviewing; **Mohamad Moustafa:** (Biological part) Conceptualization, Validation, Writing – review & editing; **Waraky, Ahmed:** (Biological part) Conceptualization, Validation, Writing – review & editing; **Darwich, Nourhane A.:** Investigation (Biological and physical part), Methodology, Data curation, Formal analysis, Software, Writing – review & editing original draft; **Khalil, Mahmoud I.:** Investigation (Biological part), Conceptualization, Methodology, Formal analysis, Validation, Writing – review & editing; **Hamdalla, Taymour A.:** Investigation, Conceptualization, Methodology, Writing – review. All authors have read and agreed to the submitted version of the manuscript.

Funding and acknowledgment. The authors extend their appreciation to the Deanship of Research and Graduate Studies at the University of Tabuk for funding this work through Research No. S-2024-0111.

Data Availability Statement. The original contributions presented in the study are included in the article. Upon request, additional information can be attained from the corresponding author.

Conflicts of interest. The authors declare no conflict of interest.

References

1. Malik, S., Muhammad, K., & Waheed, Y. (2023). Nanotechnology: a revolution in modern industry. *Molecules*, *28*(2), 661.

2. Ahmad, B., Khan, M. I., Naeem, M. A., Alhodaib, A., Fatima, M., Amami, M., Al-Abbad, E.A., Kausar, A., Alwadai, N., Nazir, A. & Iqbal, M. (2022). Green synthesis of NiO nanoparticles using Aloe vera gel extract and evaluation of antimicrobial activity. *Materials Chemistry and Physics*, *288*, 126363.
3. Alfadhli, S., Khasim, S., Darwish, A. A. A., Al-Nahdi, K., Abdelkader, M., Gamal, R., & Hamdalla, T. A. (2025). Facile green synthesis of silver doped NiO nanoparticles using aloe vera latex for efficient energy storage and photocatalytic applications. *Heliyon*, *11*(1).
4. Burduşel, A. C., Gherasim, O., Grumezescu, A. M., Mogoantă, L., Ficai, A., & Andronescu, E. (2018). Biomedical applications of silver nanoparticles: an up-to-date overview. *Nanomaterials*, *8*(9), 681.
5. Rizwana, H., Bokahri, N. A., S. Alkhattaf, F., Albasher, G., & A. Aldehaish, H. (2021). Antifungal, antibacterial, and cytotoxic activities of silver nanoparticles synthesized from aqueous extracts of mace-arils of Myristica fragrans. *Molecules*, *26*(24), 7709.
6. Hamdalla, T. A., Darwish, A. A. A., Khasim, S., Aljohani, M. M., Al-Ghamdi, S. A., El-Zaidia, E. F. M., & Alfadhli, S. (2025). Enhancing the optical and photoelectric efficiency of PEDOT/PSS thin film by incorporating activated biochar for photovoltaic applications. *Journal of Asian Ceramic Societies*, *13*(1), 36-45.
7. Singh, A. V., Vyas, V., Patil, R., Sharma, V., Scopelliti, P. E., Bongiorno, G., Podestà, A., Lenardi, C., Gade, W. N. & Milani, P. (2011). Quantitative characterization of the influence of the nanoscale morphology of nanostructured surfaces on bacterial adhesion and biofilm formation. *PloS one*, *6*(9), e25029.
8. Akram, A., Ahmad, W., Arif, M. M., Saqib, K. A., Pirzada, R. H., & Naqvi, S. Z. H. (2023). In silico docking studies of Ag nanoparticles and its derivatives against NS5B protein (HCV): Integrating nanobiotechnology and nanoinformatics. *Journal of the Pakistan Institute of Chemical Engineers*, *51*(2).
9. Ahmad, S., Munir, S., Zeb, N., Ullah, A., Khan, B., Ali, J., Bilal, M., Omer, M., Alamzeb, M., Salman, S.M., & Ali, S. (2019). Green nanotechnology: A review on green synthesis of silver nanoparticles – An ecofriendly approach. *International Journal of Nanomedicine*, 5087-5107.
10. Alharbi, N. S., Alsubhi, N. S., & Felimban, A. I. (2022). Green synthesis of silver nanoparticles using medicinal plants: Characterization and application. *Journal of Radiation Research and Applied Sciences*, *15*(3), 109-124.
11. Danks, A. E., Hall, S. R., & Schnepp, Z. J. M. H. (2016). The evolution of 'sol–gel'chemistry as a technique for materials synthesis. *Materials Horizons*, *3*(2), 91-112.
12. Chauiyakh, O., Et-Tahir, A., Kettani, K., Cherrat, A., Benayad, A., & Chaouch, A. (2022). Review on health status, chemical composition and antimicrobial properties of the four species of the genus Cedrus. *International Wood Products Journal*, *13*(4), 272-285.
13. Nayal, R., Abajy, M. Y., & Al Bakour, A. (2023). Phytochemicals and bioactivities of cedrus libani A. Rich. *Bulletin of Pharmaceutical Sciences Assiut University*, *46*(2), 881-897.
14. Makabenta, J. M. V., Nabawy, A., Li, C. H., Schmidt-Malan, S., Patel, R., & Rotello, V. M. (2021). Nanomaterial-based therapeutics for antibiotic-resistant bacterial infections. *Nature Reviews Microbiology*, *19*(1), 23-36.
15. Mohanaparameswari, S., Balachandramohan, M., Sasikumar, P., Rajeevgandhi, C., Vimalan, M., Pugazhendhi, S., Kumar, K.G., Albukhaty, S., Sulaiman, G.M., Abomughaid, M.M. & Abu-Alghayth, M. (2023). Investigation of structural properties and antibacterial activity of AgO nanoparticle extract from Solanum nigrum/Mentha leaf extracts by green synthesis method. *Green Processing and Synthesis*, *12*(1), 20230080.
16. Darwich, N. A., Mezher, M., Abdallah, A. M., Hachem, Z., El-Sayed, A. F., El Hajj, R., Hamdalla, T.A. & Khalil, M. I. (2025). Silver and Yttrium-Doped Silver Nanoparticles From Pine Needle Leaf Extract: Synthesis, Characterization, Antioxidant, Antiuropathogenic Bacterial, and Docking Activities. *Bioinorganic Chemistry and Applications*, *2025*(1), 1566870.
17. Darwich, N. A., Mezher, M., Abdallah, A. M., El-Sayed, A. F., El Hajj, R., Hamdalla, T. A., & Khalil, M. I. (2024). Biosynthesis; Characterization; and Antibacterial, Antioxidant, and Docking Potentials of Doped Silver Nanoparticles Synthesized From Pine Needle Leaf Extract. *Processes*, *12*(11), 2590.
18. Ansari, S. A., Khan, M. M., Ansari, M. O., & Cho, M. H. (2015). Silver nanoparticles and defect-induced visible light photocatalytic and photoelectrochemical performance of Ag@ m-TiO_2 nanocomposite. *Solar Energy Materials and Solar Cells*, *141*, 162-170.
19. Sun, S. K., Wang, H. F., & Yan, X. P. (2018). Engineering persistent luminescence nanoparticles for biological applications: from biosensing/bioimaging to theranostics. *Accounts of Chemical Research*, *51*(5), 1131-1143.
20. Pasieczna-Patkowska, S., Cichy, M., & Flieger, J. (2025). Application of Fourier transform infrared (FTIR) spectroscopy in characterization of green synthesized nanoparticles. *Molecules*, *30*(3), 684.
21. Harish, V., Tewari, D., Gaur, M., Yadav, A. B., Swaroop, S., Bechelany, M., & Barhoum, A. (2022). Review on nanoparticles and nanostructured materials: Bioimaging, biosensing, drug delivery, tissue engineering, antimicrobial, and agro-food applications. *Nanomaterials*, *12*(3), 457.

22. Siam, A. M., Abu-Zurayk, R., Siam, N., Abdelkheir, R. M., & Shibli, R. (2025). Forest Tree and Woody Plant-Based Biosynthesis of Nanoparticles and Their Applications. *Nanomaterials*, *15*(11), 845.
23. Abdel-Aziz, M. M., Yahia, I. S., Wahab, L. A., Fadel, M., & Afifi, M. A. (2006). Determination and analysis of dispersive optical constant of TiO_2 and Ti_2O_3 thin films. *Applied Surface Science*, *252*(23), 8163-8170.
24. Deng, R., Ozsdolay, B. D., Zheng, P. Y., Khare, S. V., & Gall, D. (2015). Optical and transport measurement and first-principles determination of the ScN band gap. *Physical Review B*, *91*(4), 045104.
25. Simonov, A., & Goodwin, A. L. (2020). Designing disorder into crystalline materials. *Nature Reviews Chemistry*, *4*(12), 657-673.
26. Ponte, R., Rauwel, E., & Rauwel, P. (2023). Tailoring SnO_2 defect states and structure: reviewing bottom-up approaches to control size, morphology, electronic and electrochemical properties for application in batteries. *Materials*, *16*(12), 4339.
27. Yakar, Y., Çakır, B., & Özmen, A. (2018). Dipole and quadrupole polarizabilities and oscillator strengths of spherical quantum dot. *Chemical Physics*, *513*, 213-220.
28. Domínguez, A. V., Algaba, R. A., Canturri, A. M., Villodres, Á. R., & Smani, Y. (2020). Antibacterial activity of colloidal silver against gram-negative and gram-positive bacteria. *Antibiotics*, *9*(1), 36.
29. Qanash, H., Bazaid, A. S., Binsaleh, N. K., Alharbi, B., Alshammari, N., Qahl, S. H., Alhuthali, H.M. & Bagher, A. A. (2023). Phytochemical characterization of Saudi mint and its mediating effect on the production of silver nanoparticles and its antimicrobial and antioxidant activities. *Plants*, *12*(11), 2177.
30. Das, B., Dash, S. K., Mandal, D., Ghosh, T., Chattopadhyay, S., Tripathy, S., Das, S. Dey, S., Das, D. & Roy, S. (2017). Green synthesized silver nanoparticles destroy multidrug resistant bacteria via reactive oxygen species mediated membrane damage. *Arabian Journal of Chemistry*, *10*(6), 862-876.
31. Girma, A., Mebratie, G., Mekuye, B., Abera, B., Bekele, T., & Alamnie, G. (2024). Antibacterial capabilities of metallic nanoparticles and influencing factors. *Nano Select*, *5*(12), e202400049.
32. Khaldoun, K., Khizar, S., Saidi-Besbes, S., Zine, N., Errachid, A., & Elaissari, A. (2025). Synthesis of silver nanoparticles as an antimicrobial mediator. *Journal of Umm Al-Qura University for Applied Sciences*, *11*(2), 274-293.
33. Mikhailova, E. O. (2024). Green silver nanoparticles: an antibacterial mechanism. *Antibiotics*, *14*(1), 5.
34. Singh, S., Singh, S. K., Chowdhury, I., & Singh, R. (2017). Understanding the mechanism of bacterial biofilms resistance to antimicrobial agents. *The Open Microbiology Journal*, *11*, 53.
35. Afrasiabi, S., & Partoazar, A. (2024). Targeting bacterial biofilm-related genes with nanoparticle-based strategies. *Frontiers in Microbiology*, *15*, 1387114.
36. Hosnedlova, B., Kabanov, D., Kepinska, M., B Narayanan, V. H., Parikesit, A. A., Fernandez, C., Bjørklund, G., Nguyen, H.V., Farid, A., Sochor, J., Pholosi, A., Baron, M., Jakubek, M. & Kizek, R. (2022). Effect of biosynthesized silver nanoparticles on bacterial biofilm changes in S. aureus and E. coli. *Nanomaterials*, *12*(13), 2183.
37. Mohanta, Y. K., Chakrabartty, I., Mishra, A. K., Chopra, H., Mahanta, S., Avula, S. K., Patowary, K., Ahmed, R., Mishra, B., Mohanta, T.K., Saravanan M. & Sharma, N. (2023). Nanotechnology in combating biofilm: A smart and promising therapeutic strategy. *Frontiers in Microbiology*, *13*, 1028086.
38. Jain, A., Jangid, T., Jangir, R. N., & shankar Bhardwaj, G. (2024). A Comprehensive Review on the Antioxidant Properties of Green Synthesized Nanoparticles: in vitro and in vivo Insights. *Free Radicals and Antioxidants*, *14*(2), 34-61.
39. Darwich, N. A., Mezher, M., Abdallah, A. M., El-Sayed, A. F., El Hajj, R., Hamdalla, T. A., & Khalil, M. I. (2024). Green Synthesis of Yttrium Derivatives Nanoparticles Using Pine Needle Leaf Extract: Characterization, Docking, Antibacterial, and Antioxidant Potencies. *Processes*, *12*(8), 1713.

Aljohani, Meshari M., Khasim, Syed, Albalawi, Mahmoud E., Alfadhli. S., Ali, Mohamad Moustafa, Waraky, Ahmed, Darwich, Nourhane A., Khalil, Mahmoud I. and Hamdalla, Taymour A. (2026). Green Synthesis of Silver and Silver Oxide Nanoparticles from *Cedrus libani*: Biological Activity and Influence of Film Thickness on Optical Properties**.** *Ukrainian Journal of Physical Optics*, *27*(1), 01080 – 01101. doi: 10.3116/16091833/Ukr.J.Phys.Opt.2026.01080

Анотація. *Наночастинки срібла та оксиду срібла (Ag/AgO-НЧ) демонструють чудові оптичні та антибактеріальні властивості, що робить їх цінними для низки промислових та біомедичних застосувань. У цьому дослідженні представлено синтез та характеристику Ag/AgO-НЧ, екстрагованих з листя Cedrus libani, з акцентом на вплив товщини плівки (100, 200 та 300 нм). Наночастинки були охарактеризовані за допомогою фотолюмінесценції (ФЛ), рентгеноструктурного аналізу (РСА),*

просвічуючої електронної мікроскопії (ПЕМ) та ІЧ Фур'є спектроскопії (ІЧФС). В спектрі ФЛ виявився пік випромінювання в околі 400 нм, що є наслідками поверхневих дефектів та фітохімічної стабілізації. ІЧФС підтвердила відновлення та кепінг функціональних груп, тоді як ПЕМ показав середній розмір частинок 20,38 нм (діапазон: 10–40 нм). Піки при 38,05°, 44,25° та 64,35° вказують на гранецентровані кубічні наночастинки Ag/AgO, що підтверджено рентгенівським дифракційним аналізом. Також спостерігалося пропускання понад 90 % при 1000 нм і вище, а також залежна від товщини плівки ширина забороненої зони 1,22–1,27 еВ. Біологічні аналізи показали значну антибактеріальну, антиоксидантну та антибіоплівкову активність. Ag/AgO-НЧ мали мінімальну інгібуючу концентрацію 0,375 мг/мл та мінімальну бактерицидну концентрацію 0,75 мг/мл проти S. aureus та E. coli. Тест на знищення з урахуванням часу показав повне пригнічення росту через 24 години. Також спостерігалося приблизно 41 % пригнічення біоплівки приблизно при субдозах, і максимум 70% попередньо сформованих біоплівок було знищено. Була оцінена антиоксидантна активність. Результати показали 59,68 % та 77,5 % поглинання радикалів при 100 та 200 мкг/мл відповідно. Таким чином, Ag/AgO-НЧ, отримані з Cedrus libani, проявляють антимікробну, антибіоплівкову та антиоксидантну активність, що підкреслює їх перспективність як для фотонних, так і для біомедичних застосувань.

Ключові слова: *наночастинки срібла та оксиду срібла, товщина плівки, оптичні властивості, антибактеріальна активність, фотонні та біомедичні застосування, ліванський кедр (Cedrus libani)*